Photonic intrinsic chiral flatband with tailorable quality factor and circular dichroism

Yuexin Sun, Shiwang Yu, Guangzhou Geng, Zhancheng Li, Yanchun Wang, Wenwei Liu, Hui Liu, Qiang Li, Junjie Li, Hua Cheng*, and Shuqi Chen**

Dr. Y. Sun, Dr. S. Yu, Prof. Z. Li, Dr. Y. Wang, Prof. W. Liu, Prof. H. Liu, Prof. H. Cheng, Prof. S. Chen
The Key Laboratory of Weak Light Nonlinear Photonics, Ministry of Education, School of Physics and TEDA Institute of Applied Physics, Nankai University, Tianjin 300071, China
E-mail: zcli@nankai.edu.cn; hcheng@nankai.edu.cn; schen@nankai.edu.cn
Dr. G. Geng, Prof. J. Li
Beijing National Laboratory for Condensed Matter Physics, Institute of Physics, Chinese Academy of Sciences, Beijing 100190, China
Prof. Q. Li, Prof. S. Chen
School of Materials Science and Engineering, Nankai University, Tianjin 300350, China
Prof. S. Chen
The Collaborative Innovation Center of Extreme Optics, Shanxi University, Taiyuan, Shanxi 030006, China

Keywords: photonic chiral flatband, Brillouin zone folding, quasi-guided modes, partially etched dielectric metasurface, nonlinear circular dichroism

Abstract: Engineering spin-selective light-matter interactions in photonic systems requires precise control of the radiative loss, optical chirality, and dispersion of resonant modes; however, these properties are intricately dependent on the structural parameters, making their independent tuning challenging. Herein, a partially etched dielectric metasurface supporting an intrinsic chiral quasi-guided mode (QGM) with flatband dispersion is proposed, for which the quality (Q) factor and circular dichroism (CD) can be independently modulated. The QGM is generated via Brillouin zone folding, with its flatband dispersion remaining robust against structural variations within a certain range. The radiative loss and spin-dependent coupling strength of the QGM can be independently engineered by adjusting the scaling ratio and rotation angle of individual nanostructures, enabling decoupled control of Q factor and CD while maintaining the flatband dispersion. Experimental measurements of the chiral QGM confirm the independent tunability of Q factor and CD, demonstrating angle-insensitive linear and nonlinear CD. Our work establishes a general physical mechanism for realizing flatband QGMs with independently tunable Q factor and CD, providing a versatile platform for next-generation functional chiral metasurfaces with potential applications in chiral emission, harmonic generation, and ultrasensitive optical sensing.

1. Introduction

Recent advances in metaphotonics have revealed the remarkable potential of all-dielectric metasurfaces for realizing nonlocal chiroptical resonances with high quality (Q) factors and near-unity circular dichroism (CD), such as chiral guided-mode resonances (GMRs)[1,2] and bound states in the continuum (BICs),[3-5] which provide a versatile platform for tailoring light-matter interactions and engineering optical fields with unprecedented flexibility.[6-8] Among them, quasi-guided modes (QGMs), a typical type of GMRs originating from the Brillouin zone folding, have attracted increasing attention due to their robust Q factors over a broad wavevector range.[9,10] These resonances enable enhanced and spin-selective light-matter interactions, paving the way for low-threshold chiral nanolasers,[11-13] ultrasensitive sensing,[14] and polarization-selective light detection.[15,16] Chiroptical resonances can be broadly classified into two categories: extrinsic and intrinsic responses.[17-23] The extrinsic chiroptical response arises from structural anisotropy or oblique incidence and does not require breaking the out-of-plane mirror symmetry.[24,25] Unlike extrinsic responses, intrinsic chiral responses exhibit spin-momentum locking, in which the spin of photon is inherently tied to the propagation momentum, leading to a CD that remains invariant under opposite illumination directions, which plays a crucial role in chiral emission control and nonlinear harmonic generation.[26,27] While extrinsic high-Q chiroptical responses can be readily achieved in planar nanostructures, realizing the intrinsic counterpart remains far more challenging. Recent progress has enabled the experimental realization of high-Q intrinsic chiral resonances through advanced nanofabrication strategies that break the out-of-plane mirror symmetry. For instance, intrinsic chiral quasi-BICs have been demonstrated in slant-perturbed metasurfaces through modulation of the eigenpolarization map in momentum space,[26,28] and in multi-height metasurfaces by controlling the coupling between electric dipole moments.[29,30] Although these approaches effectively achieve high-Q intrinsic chiral resonances and enable chiral light emission, their complex fabrication processes and strict tolerance requirements hinder broader applications.

Recent advances suggest that partially etched dielectric metasurfaces exploiting strong mode coupling or collective modal interference offer promising alternatives for realizing high-Q intrinsic chiroptical responses.[31] These structures not only feature simpler fabrication and higher precision but also allow decoupled control of the Q factor and CD, showing great potential for polarization manipulation and enhanced harmonic generation.

Furthermore, engineering the energy-momentum dispersion of nonlocal resonances provides an additional degree of freedom for tailoring light-matter interactions and controlling their coupling to free-space radiation. Among various dispersion-engineering strategies, flatband dispersions have attracted considerable attention due to their unique properties, including near-zero group velocity and a high density of states (DOS) across a broad wavevector range.[32-34] These features greatly enhance light-matter interactions while suppressing finite-size effects, thereby enabling high-Q resonances in compact devices.[35,36] Benefiting from such characteristics, flatbands have been employed in a variety of applications, including low-threshold lasing,[37,38] thermal emission,[39-41] and enhanced harmonic generation.[42-45] However, high-Q chiral resonances with flatband dispersion that enable angular-robust chiroptical functionalities have been rarely reported. The first experimental observation of an intrinsic chiral flatband with CD close to 0.6 over a wide incident-angle range (±5°) was reported very recently,[46] but its CD and Q factor remain intricately correlated with the structural geometry and cannot be independently tailored. Realizing high-Q intrinsic chiroptical resonances with flatband dispersion over larger angular ranges and independently controllable CD and Q factor, which is essential for angle-robust chiroptical functionalities, remains a challenge.

Here, we numerically and experimentally demonstrate an intrinsic chiral QGM with flatband dispersion over ±14° and independently controllable Q factor and CD in a partially etched amorphous silicon (α-Si) metasurface. The QGM arises from Brillouin zone folding induced by structural perturbations, whose flatband dispersion is inherently insensitive to variations in structural parameters. Building upon our previous work,[31] this insensitivity enables independent control of Q factor and CD via structural tuning while preserving the flatband dispersion, overcoming the previous limitation in which tuning Q and CD would compromise flatband properties and providing a versatile platform for precise manipulation of angular-robust chiroptical responses. We demonstrate that the radiative loss and the spin-dependent coupling strength of QGM can be independently controlled by two distinct structural parameters, allowing decoupled tuning of the Q factor and CD. Theoretically, CD can be varied from ±1 to 0, and the Q factor can be adjusted by more than an order of magnitude, all while preserving the flatband dispersion. The experimental results further confirm that the CD and Q factor can be effectively controlled by tuning the two structural parameters, respectively, without altering the flatband dispersion. Specifically, the CD is experimentally tuned from approximately −0.75 (averaged over the flatband range of ±14°) to 0, while maintaining flatband dispersion across the same angular range. We further experimentally demonstrate that this intrinsic chiral QGM, with angular-robust Q factor and CD, can realize angle-robust nonlinear CD. Our work provides an effective approach for achieving intrinsic chiral QGMs with flatband dispersion and independently tunable Q factors and CD, facilitating nonlinear chiral harmonic generation, enhanced chiral light emission, and ultrasensitive photonic sensing.

2. Results and Discussion

Figure 1a illustrates the angle-robust CD supported by an intrinsic chiral QGM with flatband dispersion in our partially etched α-Si metasurface. The metasurface is supported by a SiO_2 substrate, and its unit cell follows a hexagonal lattice comprising identical double-sided scythe (DSS) α-Si nanostructures ($r_1 = r_2 = 177$ nm, $\alpha_1 = \alpha_2 = 30°$, $w = 150$ nm) placed on a planar α-Si slab, as shown in Figure 1b. The period p along the x direction is 530 nm. Each resonator has a height $h_1 = 455$ nm and the slab thickness is $h_2 = 200$ nm. The DSS geometry possesses in-plane inversion (C_2) symmetry, while the underlying slab breaks the out-of-plane symmetry and enables the emergence of intrinsic chiroptical resonances. In the simulations, the refractive

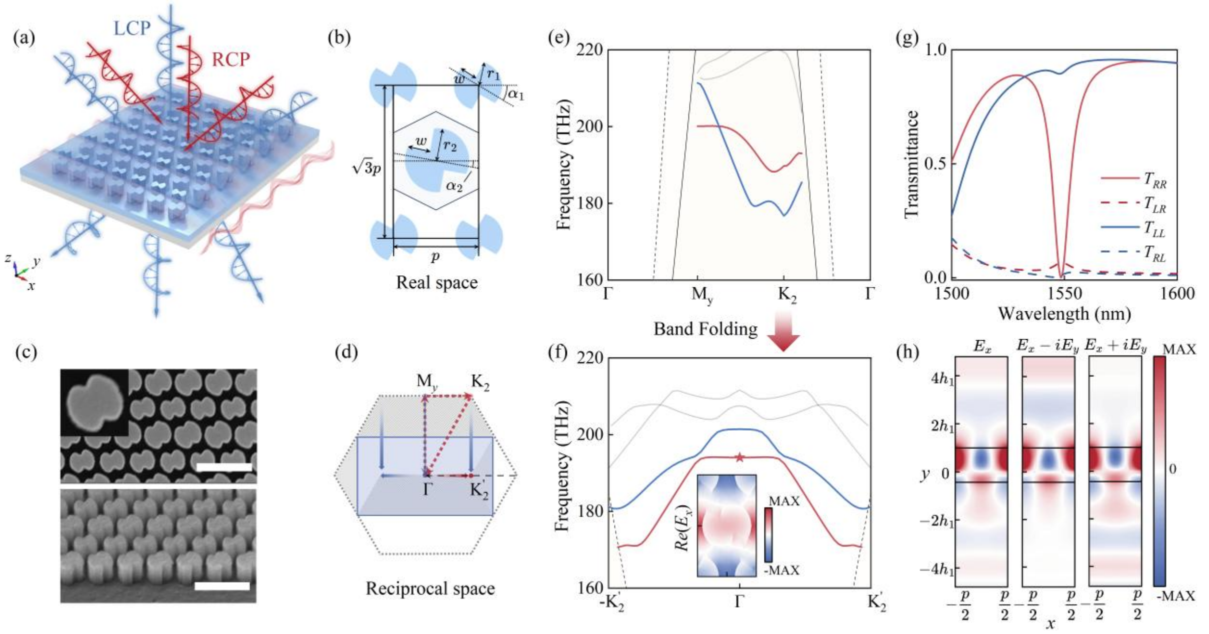

Figure 1. Schematic illustration and characterization of the intrinsic chiral QGM exhibiting unidirectional flatband dispersion in the designed partially etched dielectric metasurface. (a) Schematic of the angle-robust CD enabled by an intrinsic chiral QGM with flatband dispersion. (b) Structural configuration of the metasurface. (c) The top-view and cross-sectional SEM images of the metasurface. Scale bars, 1 μm. (d) Evolution of the first Brillouin zone, where the blue rectangle denotes the perturbed zone and the shaded regions highlight the folding domains. (e) Band structure of the metasurface with unperturbed lattice plotted along Γ-M_y-K_2. (f) Band structure of the perturbed metasurface along $-K_2'$-Γ-K_2', with the emerging flatband QGM highlighted in red. The inset shows the real part of the *x*-component of the electric field on the *x*-*y* plane (on the middle section of the structures) at the Γ point. The solid and dashed lines in (e) and (f) denote the light cones of the substrate and air, respectively. (g) The simulated transmission spectra at the Γ point, corresponding to the position marked by the red star in (f). T_{ij} denotes the square of the amplitude of the transmission coefficient from an incident circularly polarized (CP) state *j* to a transmitted state *i*. (h) Electric field profiles of the QGM at the Γ point, showing that the mode predominantly radiates upward into RCP light. Notably, the color is saturated for better illustration of the radiation field.

index of α-Si was taken from experimental data (Supporting information (SI), Figure S1), while the refractive index of SiO_2 was set to 1.45. To match the experimental fabrication conditions (Figure 1c), a 4° inclined sidewall and rounded edges were incorporated into the simulations.

To access the desired QGM, we apply a targeted perturbation to the central nanostructures (r_2 = 205 nm, α_2 = 10°), which deforms the original hexagonal unit cell into a rectangular one. This structural modification folds the Brillouin zone from the dashed grey hexagon to the solid blue rectangle (Figure 1d), thereby generating the flatband QGM. Specifically, when these two structures share identical geometry parameters ($r_1 = r_2$, $\alpha_1 = \alpha_2$), the corresponding band structure in Figure 1e shows that the modes of interest along the M_y-K_2 direction lie entirely below the light line, indicating that they are non-radiative guided modes (GMs). Along this direction, a nearly dispersionless band segment emerges, originating from the standing-wave character of the modes at the Brillouin zone boundary. Such modes inherently maintain their flatband dispersion even when the structural parameters are varied within a reasonable range. This stability provides a robust basis for tuning the CD magnitude and the Q factor without altering the band dispersion, enabling simple and fabrication-friendly strategies for realizing and engineering chiroptical resonances. Two optional perturbations can be applied to the central DSS elements (marked by the hexagon in Figure 1b) to enable the excitation of the flatband mode from free space: (i) adjusting the scaling ratio through variation of r_2 ($\delta = r_2 - r_1$), and (ii) modifying the rotation angle α_2 relative to α_1 ($\alpha_2 \neq \alpha_1$). These two perturbations equivalently induce Brillouin zone folding, as they modify the local geometry without changing the period of the folded lattice. As a result, the GMs along the M_y-K_2 direction are folded onto the Γ-K_2' direction, forming QGMs that can couple to external radiation. The folded band structure (Figure 1f) exhibits a flatband dispersion along the k_x direction, with the mode of interest highlighted by a red line. This flatband is intrinsically determined by the original dispersion of the GMs, while coupling to nearby modes further constrains its angular extent. The electric field distribution in the inset of Figure 1f confirms that the QGM is a TE-like mode. To further validate the flatband behaviour, the group velocity (v_g) of the QGM band is calculated and remains near zero across the dispersionless region (SI, Figure S2). In addition, strong couplings are observed between adjacent resonant modes marked by the blue and red lines in the folded band. Notably, unlike recent approaches that attribute flatband formation to such strong couplings,[32,44] here the observed coupling has a negligible impact on the band dispersion, slightly affecting only the extent of the flatband (SI, Figure S2). Based on the calculated band structures and the corresponding Q factors, we further derive the DOS for these two adjacent resonant modes (SI, Section 3). The results indicate that, when the Q factors are comparable, the flatband mode exhibits a significantly enhanced DOS.

As shown in Figure 1g, the intrinsic chiroptical response of the flatband QGM is further validated through simulated transmission spectra under normal incidence, corresponding to the mode marked by the red star in Figure 1f. The spectra clearly demonstrate the intrinsic chiroptical nature of the QGM, as evidenced by the near-complete suppression of the cross-polarized components T_{LR} and T_{RL}. The difference between the co-polarized components T_{LL} and T_{RR} indicates the emergence of near-unity CD values, defined as $\left(T_{RCP}-T_{LCP}\right)/\left(T_{RCP}+T_{LCP}\right)$, where $T_{RCP/LCP}$ denote the transmission intensities under right- and left-handed circularly polarized (RCP and LCP) illumination, respectively. Here, we assume an $e^{i\omega t}$ time dependence of electromagnetic fields, and RCP and LCP waves are defined such that the electric field at a fixed position z rotates in a clockwise or counterclockwise direction, respectively, when viewed from the direction toward which the wave is approaching. This intrinsic chiral behavior is further confirmed by the radiated electric field components at the marked k-point, as shown in Figure 1h and represented as the real part of $E_x \pm iE_y$. The distribution reveals that the polarization state of the radiated field remains unchanged under reversal of the radiation direction, indicating that the QGM couples exclusively to RCP illumination. The intrinsic chirality is further verified by the spectral response remaining unchanged across the flatband range (SI, Section 4).

Notably, introducing perturbations to the central DSS nanostructures enables Brillouin zone folding, while within a finite parameter range, r_2 and α_2 affect the radiation field of QGM in distinct ways. Here, we employ temporal coupled mode theory (TCMT) to make a quantitative analysis. The unit cell of the perturbed metasurface can be viewed as comprising two DSS nanostructures, as illustrated in **Figures 2**a and 2b. These structures are located at opposite phase nodes of the TM-like QGM with standing-wave character. The light scattered by these two DSS nanostructures are in different elliptically polarized states, and the radiation field can be expressed as the coherent superposition of these two contributions (SI, Section 5). The results indicate that α_2 primarily governs the polarization state, whereas r_2 controls the radiation intensity, thereby enabling decoupled manipulation of the CD and Q factor of the QGM. For clarity, we decompose the upward and downward leaking states in the circularly polarized basis as follows:

$$|e_u\rangle = d_R(r_2,\alpha_2)\mathbf{e}_R + d_L(r_2,\alpha_2)\mathbf{e}_L \tag{1}$$

$$|e_d\rangle = d'_R(r_2,\alpha_2)\mathbf{e}_R + d'_L(r_2,\alpha_2)\mathbf{e}_L \tag{2}$$

where $\mathbf{e}_R$ and $\mathbf{e}_L$ correspond to RCP and LCP states, respectively, and $d_R(r_2,\alpha_2)$ ($d'_R(r_2,\alpha_2)$) and $d_L(r_2,\alpha_2)$ ($d'_L(r_2,\alpha_2)$) are the complex coupling coefficients from the QGM to the upward (downward) radiation channel in the circularly polarized bases. Specifically, the polarization states and coupling intensities of the upward and downward radiation exhibit nearly identical evolution under structural perturbations. Therefore, for clarity and without loss of generality, we focus on the upward radiation in the following analysis. The radiation intensity in the upward direction is in direct proportion to $|d_R(r_2,\alpha_2)|^2 + |d_L(r_2,\alpha_2)|^2$, which is intrinsically linked to the radiative decay rate γ. As shown in Figure 2c, the radiated intensity remains nearly unaffected by variations in α_2, while it can be effectively modulated by adjusting r_2. This indicates the changes in the scaling ratio (represented by r_2) enable effective control of

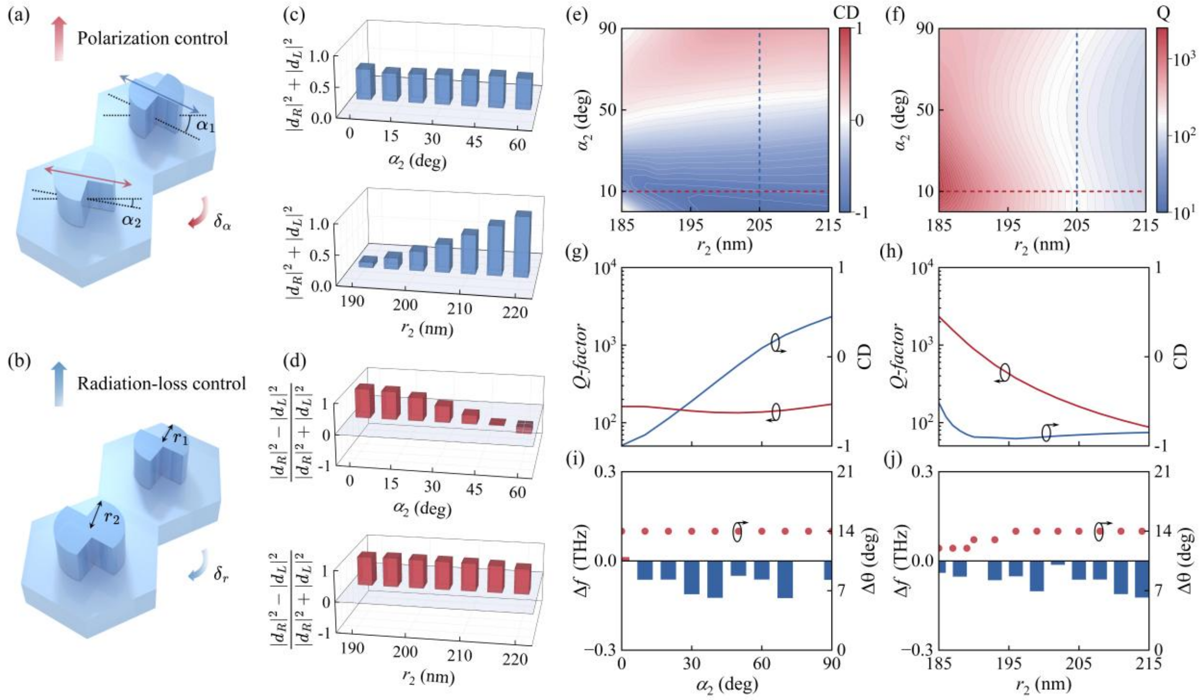

Figure 2. Decoupled manipulation of the Q factor and CD of the flatband QGM. Schematic illustration of the physical mechanism underlying the decoupled control. (a) The rotation angle α_2 tunes the polarization state of the radiative fields, causing a difference in coupling strength under LCP and RCP incidence and thereby modulating the CD. (b) The radius r_2 controls the radiative loss, enabling independent adjustment of the Q factor. (c) The radiation intensity in the upward direction as a function of α_2 (r_2 = 205nm) and r_2 (α_2 = 10°). (d) The normalized difference in coupling strengths as functions of α_2 and r_2. (e, f) Simulated CD and Q factor as functions of α_2 and r_2. (g, h) Extracted CD and Q factor along the blue (r_2 = 205 nm) and red (α_2 = 10°) dashed lines in (e) and (f). (i, j) Dispersion features of the QGM, showing Δf and $\Delta\theta$ versus α_2 and r_2, where $\Delta f = f_{\max} - f_{\min}$ denotes the frequency spacing, and $\Delta\theta$ is the angular bandwidth corresponding to a dispersion variation within 2 nm.

the Q factor, as $Q = \omega_0/2\gamma$. Meanwhile, the CD of QGM is correlated with the difference in coupling strengths $\left(\left|d_R\left(r_2,\alpha_2\right)\right|^2-\left|d_L\left(r_2,\alpha_2\right)\right|^2\right)\Big/\left(\left|d_R\left(r_2,\alpha_2\right)\right|^2+\left|d_L\left(r_2,\alpha_2\right)\right|^2\right)$. As shown in Figure 2d, this quantity can be tuned by α_2, while remaining nearly constant with variation in r_2, indicating the changes in the rotation angle α_2 enable effective control of the CD of QGM.

To visually characterize the decoupled manipulation of the Q factor and CD of the QGM through variations in r_2 and α_2, we simulated their dependence across the r_2-α_2 parameter space, as shown in Figures 2e and 2f. The results show that the CD varies almost monotonically with increasing α_2 while remaining largely insensitive to changes in r_2. In contrast, the Q factor exhibits the opposite behavior. To enable a quantitative assessment, the variations of CD and Q factor along the trajectories indicated by the blue and red dashed lines in Figures 2e and 2f are plotted in Figures 2g and 2h. Along the blue dashed line, where r_2 is held constant, the CD can be tuned from −1 to 0.5 as α_2 increases from 0° to 90°, while the Q factor remains nearly constant at approximately 160. By employing the mirror-symmetric counterpart of the metasurface, the CD range extends from −0.5 to 1, enabling full tunability from ±1 to 0 (SI, Figure S6). Along the red dashed line, where α_2 remains fixed, the Q factor decreases as r_2 increases from 185 nm to 215 nm, whereas the CD stays close to unity. Because $\delta = r_2 - r_1$ serves as a typical asymmetric parameter for QGMs, the variation of Q factor with r_2 follows an inverse quadratic dependence.[47-49] These results confirm that the CD and Q factor of the QGM can be independently controlled by adjusting α_2 and r_2, respectively. Importantly, because the flatband dispersion of QGM originates from the standing-wave nature of the corresponding GM at the Brillouin zone boundary, variations in α_2 and r_2 exert only minimal influence on the band structure. As illustrated in Figures 2i and 2j, the frequency deviation Δf, defined as the frequency difference between the upper and lower edges of the QGM within the flatband region, remains below 0.2 THz (corresponding to a wavelength shift of less than 2 nm), and the corresponding angular width $\Delta\theta$ remains at 12° or wider. These results clearly demonstrate that the QGM supports independent tuning of CD and Q factor while preserving robust flatband resonance, as further confirmed by angle-resolved CD in Section 7, SI. Notably, other structural parameters, such as the etch width w, can also affect the Q factor by modifying the effective scaling ratio of the nanostructure. Meanwhile, the CD remains unchanged, and the flatband dispersion is well preserved (SI, Section 8).

To experimentally validate the chiral QGM with flatband dispersion and the decoupled control of the Q factor and CD, we fabricated two series of partially etched α-Si metasurfaces with different α_2 and r_2. To characterize the tunability of CD, we fabricated samples with $\alpha_2 = 10°$, 35°, and 55° while keeping $r_2 = 205$ nm, corresponding to target CD values of −1, −0.5, and 0, respectively. **Figures 3**a(i-iii) and 3b show the simulated and measured angle-resolved transmission spectra, respectively. The measurements confirm the formation of flatband dispersion over an incident angular range of ±14° (the region between the dashed lines in Figure 3b) for samples with different α_2, in good agreement with simulated results. The modest discrepancies between the experimental and simulated results are mainly attributed to fabrication imperfections affecting structural parameters, and to fabrication-induced nonuniformities across the sample area (SI, Section 8). The experimentally measured CD values for each rotation angle are summarized in Figure 3c, demonstrating that CD can be systematically tuned via controlled variation of α_2. Figure 3d shows the Q factor of the QGM, extracted from the measured transmission spectra using Fano resonance fitting, illustrating that the Q factor remains nearly constant at $Q \approx 95$, with only minor deviations observed at larger incident angles for $\alpha_2 = 10°$. These results confirm that increasing α_2 reduces CD while preserving the stability of the Q factor. The dependence of the Q factor on r_2 has been further demonstrated by measuring the angle-resolved transmission spectra of the fabricated samples with $r_2 = 195$ nm and 205 nm while $\alpha_2 = 10°$, shown in Figures 3a(i) and 3a(iv). The results validate that the flatband dispersion is well preserved within ±14°. As r_2 increases from 195 nm to 205 nm, the Q factor drops by nearly half across the entire wavevector range (Figure 3e). Notably, while the designed CD at the resonant wavelength remains unchanged, slight variations are observed experimentally for different r_2 (SI, Figure S9). Moreover, the flatband dispersion is well preserved across the structural variations. As shown in Figure 3f, the resonance shift $\Delta\lambda$ is extracted, revealing that within the ±14° incident range, the resonance

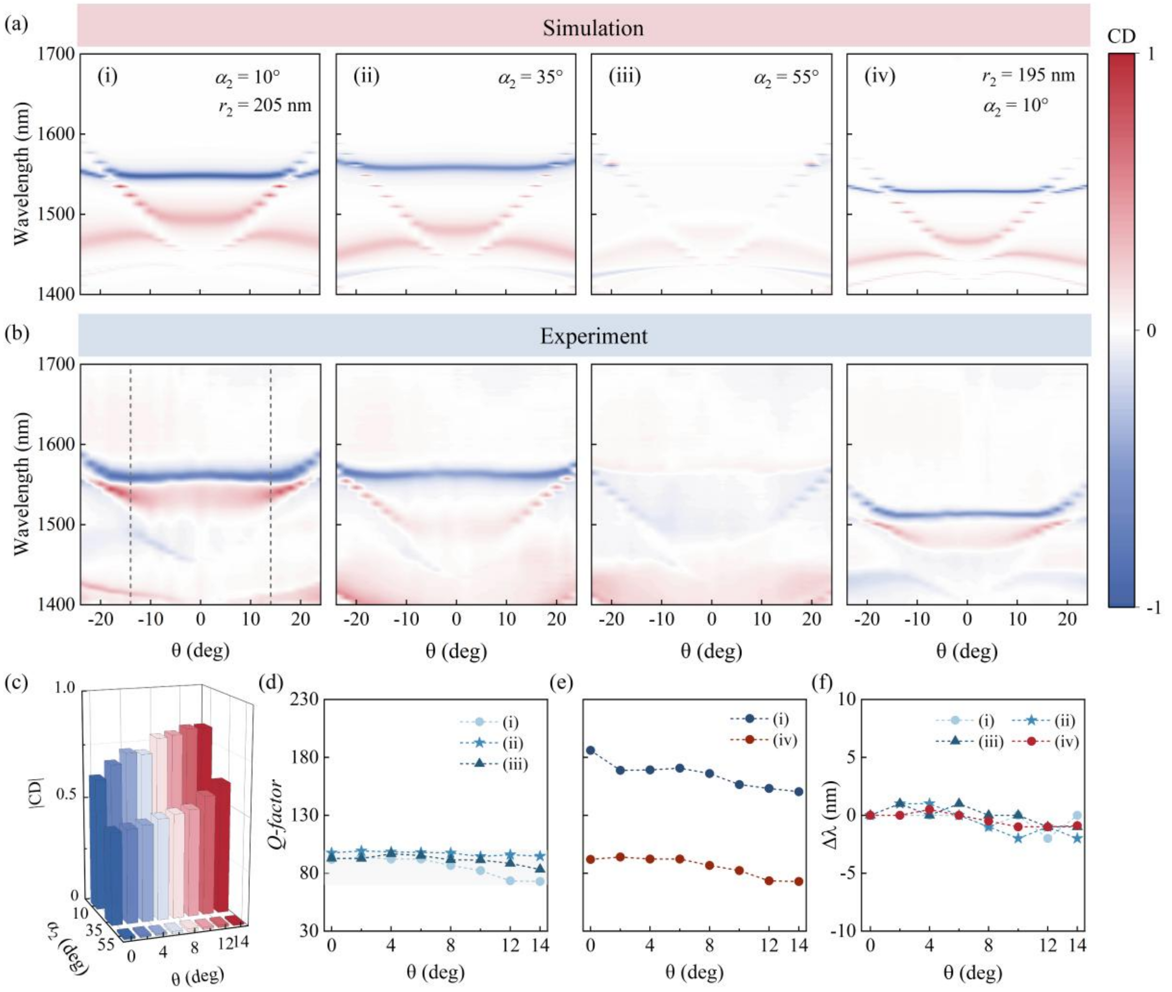

Figure 3. Experimental demonstration of the flatband QGM with decoupled tuning of CD and Q factor. (a, b) Simulated and measured angle-resolved CD spectra for (i) $\alpha_2 = 10°$, (ii) 35°, and (iii) 55° with $r_2 = 205$ nm, and for (iv) $r_2 = 195$ nm with $\alpha_2 = 10°$. (c) Extracted CD at the resonance for different incident angles. Bar colors indicate different incident angles. (d, e) Extracted Q factor at the resonance for different incident angles. (f) Measured Δλ for different incident angles, where $\Delta\lambda = \lambda_{max} - \lambda_0$ denotes the resonance shift and λ_0 is the resonant wavelength at $\theta = 0°$.

positions shift by less than 2 nm. Overall, these experimental findings substantiate the realization of a chiral QGM with flatband dispersion and its versatile tunability.

The proposed flatband QGM enables not only linear chiral optical manipulation but also holds significant potential for nonlinear chiral nanophotonics, which is essential for ultrafast spin control and spin-dependent quantum light generation. The nonlinear chirality originates from the spin-dependent enhancement of the electric field. **Figure 4**a depicts the electric field magnitude (|*E*|) distributions at normal incidence for RCP and LCP excitations. Specifically, the electric field enhancement (*FE*) was quantified, demonstrating that the enhancement under RCP excitation exceeds that under LCP excitation by a factor of approximately 30. The *FE* of the structure is defined as:

$$FE_{avg} = \frac{\iiint (E / E_0)^2 dV}{V}, \tag{3}$$

where the integration volume V encompasses the entire structure, E denotes the amplitude of the electric field, and E_0 represents the amplitude of the incident wave. Exploiting this spin-dependent electric field enhancement of the flatband QGM, we experimentally demonstrate angle-robust chiral third-harmonic generation (THG) with near-unity CD. To illustrate the angular robustness of the nonlinear CD more clearly, we also consider the THG response under oblique incidence along the *y*-direction, which corresponds to a dispersion band of QGM, as a reference. Figure 4b shows the variation of the resonant wavelength of QGM with oblique incidence along both *x*- and *y*-directions. The measured THG intensities under RCP and LCP pumping along these two directions are presented in Figures 4c and 4d. The results indicate that the THG intensity remains nearly constant for incident angles up to 10° along the *x*-direction, whereas it gradually decreases along the *y*-direction. Meanwhile, the THG intensity under RCP pumping is significantly higher than that under LCP pumping across a broad angular range, resulting in an angular-robust nonlinear CD of up to 0.8 (Figure 4e). Here, the nonlinear CD is defined as $\left(I_R^{3\omega} - I_L^{3\omega}\right)/\left(I_R^{3\omega} + I_L^{3\omega}\right)$, where $I_{R/L}^{3\omega}$ denotes the THG intensity under RCP (LCP) excitation. Notably, as the THG intensity under oblique incidence along the *y*-direction nearly vanishes at 10°, restricting the angular range for comparison to values below this threshold is sufficient to elucidate the chiral contrast between the flatband and dispersive bands. In contrast,

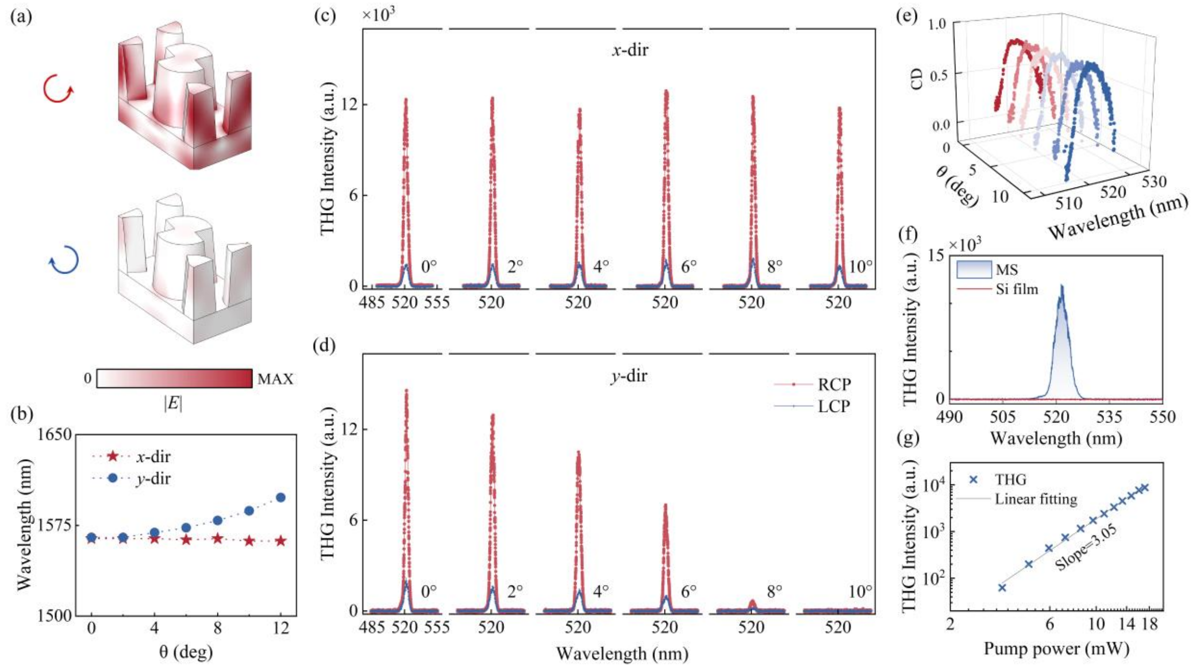

Figure 4. Experimental demonstration of angle-robust nonlinear CD based on the intrinsic chiral QGM with flatband dispersion. (a) The electric field magnitude (|*E*|) distributions at the resonance wavelength under normal incidence for RCP and LCP incidence, respectively. (b) Resonance wavelength of the fabricated metasurface as a function of the incident angle θ along the *x* and *y* directions, measured with a 2° scanning step. (c, d) Measured THG intensities under RCP and LCP excitation along the (c) *x* and (d) *y* directions at different incident angles. (e) Calculated nonlinear CD spectra derived from the measured data in (c). The color of each spectrum corresponds to a specific incident angle. (f) THG intensity under RCP incidence for the metasurface (blue) compared with the unpatterned *α*-Si film (red). (g) Log-log plot of the THG signal versus incident power. Blue crosses represent measured data, and the gray line shows a fit to a third-order power function.

for oblique incidence along the *x*-direction, the THG response remains remarkably robust, with the maximum nonlinear CD persisting up to 13°, closely approaching the angular extent of the flatband dispersion at the fundamental frequency. In addition to enabling nonlinear CD, the THG signal is significantly enhanced by the QGMs compared to a reference unpatterned *α*-Si film, reaching nearly 1.2×10^4 (Figure 4f). The measured THG conversion efficiency is approximately 1.1 × 10^{-9} for an average pump power of 15.42 mW (SI, Section 10). Figure 4g presents a log-log plot of the THG intensity versus average pump power at the resonance wavelength, with a slope of 3.05, further confirming the cubic dependence characteristic of the third-order nonlinear process.

3. Conclusion

To overcome the limited incident-angle tolerance of conventional nonlocal metasurfaces and enhance light-matter interactions, flatband modes have attracted considerable attention. In previously reported studies, flatband responses have been realized across multiple spectral ranges and in various photonic systems, as summarized in Table S1 of SI. These studies have demonstrated the capability of flatband systems to achieve high-Q resonances and enable manipulation of the Q factor. In chiral flatband modes, however, the CD and Q factor are generally tightly correlated with the same structural perturbations. Adjusting a given parameter to improve one property often degrades the others, and it can also affect the bandwidth of the flatband, making it challenging to simultaneously achieve a high Q factor, strong CD, and flexible control over all these characteristics. We introduce an intrinsic chiral QGM that exhibits a more robust flatband against structural perturbations, enabling decoupled control of the Q factor and CD. By introducing two independent structural parameters, we realize decoupled control of these two quantities while maintaining nearly unchanged band dispersion. Maintaining flatband dispersion over ±14°, we experimentally demonstrated that the CD can be tuned from approximately −0.75 to 0 with a Q factor of 95, while the Q factor can be tuned from 95 to 186 while preserving high CD. All values are averaged over the flatband range of ±14°. Further improvements in fabrication accuracy are expected to enhance the CD toward ±1 and bring the performance closer to the simulated values. Such independent tunability is particularly important for chiral resonance, as tuning the Q factor enables optimization of light-matter interaction strength, while independent control of CD provides a high degree of flexibility in engineering the radiation field. Moreover, owing to the scalable nature of the design, this chiral flatband QGM can be shifted to other spectral ranges, such as the visible regime (SI, Section 12), providing a straightforward strategy for practical nanophotonic applications.

In summary, we have numerically and experimentally demonstrated that a partially etched α-Si metasurface can support an intrinsic chiral QGM featuring flatband dispersion with independently tunable Q factor and CD. We revealed that the flatband dispersion originates from the standing-wave nature of the corresponding GM at the Brillouin zone boundary. The Q factor and CD, which are determined by the radiative loss and the spin-dependent coupling strength of the QGM, can be independently controlled by adjusting the scaling ratio and rotation angle of the nanostructures through two structural parameters. Importantly, variations in these parameters exert minimal influence on the band dispersion, enabling the realization of chiral flatband modes with adjustable Q factor and CD. Furthermore, we experimentally verified that the intrinsic chiral QGM facilitates angle-robust nonlinear chiroptical responses, as evidenced by THG exhibiting a CD exceeding 0.8 across a broad angular range. These findings establish a versatile and robust design strategy for realizing intrinsic chiral flatband QGMs with independently controllable Q factors and CD, opening pathways toward high-performance linear and nonlinear chiral photonic components in integrated nanophotonic platforms.

4. Experimental Section

Sample Fabrication: The partially etched α-Si metasurfaces, comprising DSS nanostructures on a thin slab, were fabricated on fused-quartz substrates using plasma-enhanced chemical vapor deposition (PECVD), electron-beam lithography (EBL), and reactive-ion etching (RIE). A 655-nm-thick α-Si layer was first deposited by PECVD at 120 °C using SiH_4 (10 sccm) and Ar (475 sccm) as precursor and carrier gases, respectively, with a chamber pressure (650 mTorr) and RF power of 20 W. A 455-nm polymethyl methacrylate (PMMA) resist was then spin-coated and overlaid with a thin PEDOT:PSS conductive film. After exposure on a JEOL 6300FS EBL system at a base dose of 1000 $\mu C\ cm^{-2}$ and 100 kV acceleration voltage, the conductive layer was removed by deionized-water rinsing. The resist was developed in a 1:3 MIBK:IPA solution for 40 s and subsequently rinsed in IPA for 30 s. A 100-nm chromium (Cr) hard mask was deposited by electron-beam evaporation, followed by a lift-off step in warm acetone to define the patterned Cr mask. The α-Si layer was subsequently etched through this Cr mask using RIE, where the etch duration was precisely controlled to achieve a partial etch depth of 200 nm. Finally, the remaining Cr mask was removed using a ceric ammonium nitrate solution.

Experimental Measurement: The angle-resolved transmission spectra were measured using a home-built optical setup. A supercontinuum laser (SC-Pro-M-40, YSL Photonics) served as the broadband excitation source. Circular polarization was generated using a broadband polarizer (Codixx AG, IR 1300 BC5) and an achromatic quarter-wave plate (B. Halle Nachfl, $\lambda/4$ super achromatic waveplate). The beam was then illuminated onto the sample, and the transmitted light was collected by an objective lens (Sigma NIR Plan Apo 20×, NA = 0.45). The transmitted signal was analysed using a second quarter-wave plate and polarizer to select the co-polarized component, and then directed through an aperture and a lens ($f = 100$ mm) into an optical spectrum analyzer (Zolix, Omni-750i) via a fiber coupler. The aperture defined the collection area, slightly smaller than the sample size. A flip mirror positioned after the lens enabled switching between spectral acquisition and sample imaging, which was recorded by a CMOS camera (TUCSEN, Mlchrome 5BW). The sample was mounted on a five-dimensional (5D) rotation stage to enable angle-resolved measurements. All transmission spectra were normalized to the air background. For THG measurements, the linear and nonlinear optical pathways were co-aligned within a shared platform to ensure strict beam collinearity and experimental consistency. A femtosecond laser (FLINT FL1) was used to pump an optical parametric oscillator (OPO), generating signal pulses (≈200 fs, 75.4 MHz) tunable from 1400 to 2000 nm. The excitation beam was converted to circular polarization using the same linear polarizer and achromatic quarter-wave plate employed in the linear measurements and was focused onto the metasurface by an objective lens (Sigma NIR Plan Apo 5×, NA=0.15). THG emission from the sample was collected through an objective lens (Sigma NIR Plan Apo 20×, NA = 0.45) and passed through a cascade of short-pass filters to remove residual fundamental light. The filtered THG output was subsequently coupled into an Andor spectrometer for spectral analysis.

Supporting Information

Supporting Information is available from the Wiley Online Library or from the author.

Acknowledgments

(This work was supported by the National Key Research and Development Program of China (2021YFA1400601 and 2024YFA1409903), the National Natural Science Foundation of China (W2441005, 12192253, 12274237, 12274239, 12474331, 12534014, 12547181, and U22A20258), and the National Natural Science Foundation of Tianjin (23JCQNJC01450 and 25JCYBJC01300).)

Conflict of Interest

The authors declare no conflicts of interest.

Data Availability Statement

The data that support the findings of this study are available from the corresponding author upon reasonable request.

Received: ((will be filled in by the editorial staff))
Revised: ((will be filled in by the editorial staff))
Published online: ((will be filled in by the editorial staff))

References

[1] X. Huang, Q. Lin, S.-X. Xia, X. Zhai, G.-D. Liu. Dynamic polarization control of strongly coupled quasi-guided modes enables high-efficiency THG. *Opt. Express* **2025**, *33*, 48707–48716.

[2] W. Xun, K. Sun, E. Maqbool, Z. Han. High-Q Chiral Metasurfaces: Broadband Spectral Tunability with Angle-Dependent Response. *Adv. Opt. Mater.* **2025**, *13*, 2500713.

[3] Q.-K. Liu, Y. Li, Z. Lu, Y. Zhou, W. M. Liu, X.-Q. Luo, X.-L. Wang. Steerable chiral optical responses unraveled in planar metasurfaces via bound states in the continuum. *Phys. Rev. B* **2023**, *108*, 155410.

[4] J. L. Pura, B. Castillo López de Larrinzar, M. Liang, A. García-Martín, J. Gómez Rivas, J. A. Sánchez-Gil. Superchiral Light Emerging from Bound States in the Continuum in Metasurfaces of Si Nanorod Dimers. *ACS Photonics* **2024**, *11*, 4090–4100.

[5] X. Du, L. Xiong, X. Zhao, S. Chen, J. Shi, G. Li. Dual-band bound states in the continuum based on hybridization of surface lattice resonances. *Nanophotonics* **2022**, *11*, 4843–4853.

[6] T. T. H. Do, R. Lin, D. A. Shilkin, Z. Yuan, C. Dang, A. I. Kuznetsov, J. Teng, S. T. Ha. Emerging landscape of photonic bound states in the continuum for next-generation metadevices. *Opto-Electron. Adv.* **2026**, *9*, 250224.

[7] W. Liu, Z. Li, M. A. Ansari, H. Cheng, J. Tian, X. Chen, S. Chen. Design Strategies and Applications of Dimensional Optical Field Manipulation Based on Metasurfaces. *Adv. Mater.* **2023**, *35*, 2208884.

[8] J. Yu, W. Yao, M. Qiu, Q. Li, *Light Sci. Appl.* **2025**, *14*, 174.

[9] K. Sun, H. Wei, W. Chen, Y. Chen, Y. Cai, C. W. Qiu, Z. Han. Infinite-Q guided modes radiate in the continuum. *Phys. Rev. B* **2023**, *107*, 115415.

[10] K. Sun, U. Levy, Z. Han. Exploiting zone-folding induced quasi-bound modes to achieve highly coherent thermal emissions. *Nano Lett.* **2024**, *24*, 764.

[11] H. Deng, X. Jiang, Y. Zhang, Y. Zeng, H. Barkaoui, S. Xiao, S. Yu, Y. Kivshar, Q. Song. Chiral lasing enabled by strong coupling. *Sci. Adv.* **2025**, *11*, eads9562.

[12] X. Duan, B. Wang, K. Rong, C. L. Liu, V. Gorovoy, S. Mukherjee, V. Kleiner, E. Koren, E. Hasman. Valley-addressable monolayer lasing through spin-controlled Berry phase photonic cavities. *Science* **2023**, *381*, 1429–1432.

[13] Y. Chen, M. Wang, J. Si, Z. Zhang, X. Yin, J. Chen, N. Lv, C. Tang, W. Zheng, Y. Kivshar, C. Peng. Observation of chiral emission enabled by collective guided resonances. *Nat. Nanotechnol.* **2025**, *20*, 1–8.

[14] L. Huang, R. Jin, C. Zhou, G. Li, L. Xu, A. Overvig, F. Deng, X. Chen, W. Lu, A. Alu, A. E. Miroshnichenko. Ultrahigh-Q guided mode resonances in an All-dielectric metasurface. *Nat. Commun.* **2023**, *14*, 3433.

[15] T. Jia, Y. Jeon, L. Feng, H. Kim, B. Li, G. Rui, J. Rho. Superchirality induced ultrasensitive chiral detection in high-Q optical cavities. *Opto-Electron. Adv.* **2025**, *8*, 250079.

[16] J. Hong, J. van de Groep, N. Lee, S. J. Kim, P. Lalanne, P. G. Kik, M. L. Brongersma. Nonlocal metasurface for circularly polarized light detection. *Optica* **2023**, *10*, 134–141.

[17] B. Wang, T. Zhu, Y. Liu, H. Yang, R. Pan, J. Li. Chiral Resonant Modes Induced by Intrinsic Birefringence in Lithium Niobate Metasurfaces. *Phys. Rev. Lett.* **2025**, *134*, 113802.

[18] S. A. Asefa, S. Shim, M. Seong, D. Lee. Chiral Metasurfaces: A Review of the Fundamentals and Research Advances. *Appl. Sci.* **2023**, *13*, 10590.

[19] Q.-M. Deng, X. Li, M.-X. Hu, F.-J. Li, X. Li, Z.-L. Deng. Advances on broadband and resonant chiral metasurfaces. *Npj Nanophotonics* **2024**, *1*, 1–22.

[20] W. Fei, C. Bi, L. Chen, X. Jiang, Y. Yu, Y. Chen, Q. Zhan, J. Hu. Chirality-induced strong coupling of leaky guided modes in a dielectric metasurface waveguide governed by symmetry breaking. *Opt. Express* **2025**, *33*, 16952–16964.

[21] D. Zhang, T. Liu, L. Lei, W. Deng, T. Wang, Q. Liao, W. Liu, S. Xiao, T. Yu. Tailoring intrinsic chirality in a two-dimensional planar waveguide grating via quasibound states in the continuum. *Phys. Rev. B* **2024**, *109*, 205403.

[22] Z. Li, W. Liu, H. Cheng, D. Choi, S. Chen, J. Tian. Spin-Selective Full-Dimensional Manipulation of Optical Waves with Chiral Mirror. *Adv. Mater.* **2020**, *32*, 190798.

[23] L. Zhu, Y. Zhang, G. Yang, R. Jin, C. Wang, Y. Wang, G. Li, T. Sang. Observation of Dual-Band Intrinsic Chirality in Underetched Silicon Metasurfaces via Quasi-BICs. *Nano Lett.* **2026**, *26*, 4822.

[24] W. Chen, Q. Yang, Y. Chen, W. Liu. Extremize Optical Chiralities through Polarization Singularities. *Phys. Rev. Lett.* **2021**, 126, 253901.

[25] T. Shi, Z. L. Deng, G. Geng, X. Zeng, Y. Zeng, G. Hu, A. Overvig, J. Li, C. W. Qiu, A.

Alu, Y. S. Kivshar, X. Li. Planar chiral metasurfaces with maximal and tunable chiroptical response driven by bound states in the continuum. *Nat. Commun.* **2022**, *13*, 4111.

[26] X. Zhang, Y. Liu, J. Han, Y. Kivshar, Q. Song. Chiral emission from resonant metasurfaces. *Science* **2022**, *377*, 1215–1218.

[27] I. Toftul, P. Tonkaev, K. Koshelev, F. Lai, Q. Song, M. Gorkunov, Y. Kivshar. Chiral Dichroism in Resonant Metasurfaces with Monoclinic Lattices. *Phys. Rev. Lett.* **2024**, *133*, 216901.

[28] Y. Chen, H. Deng, X. Sha, W. Chen, R. Wang, Y.-H. Chen, D. Wu, J. Chu, Y. S. Kivshar, S. Xiao, C.-W. Qiu. Observation of intrinsic chiral bound states in the continuum. *Nature* **2023**, *613*, 474–478.

[29] L. Kühner, F. J. Wendisch, A. A. Antonov, J. Bürger, L. Hüttenhofer, L. de S. Menezes, S. A. Maier, M. V. Gorkunov, Y. Kivshar, A. Tittl. Unlocking the out-of-plane dimension for photonic bound states in the continuum to achieve maximum optical chirality. *Light Sci. Appl.* **2023**, *12*, 250.

[30] Y. Tang, Y. Liang, J. Yao, M. K. Chen, S. Lin, Z. Wang, J. Zhang, X. G. Huang, C. Yu, D. P. Tsai. Chiral Bound States in the Continuum in Plasmonic Metasurfaces. *Laser Photonics Rev.* **2023**, *17*, 2200597.

[31] Z. Li, S. Yu, G. Geng, J. Cheng, W. Liu, Y. Zhang, J. Li, H. Cheng, S. Chen. Chiral Guided Mode Resonance with Independently Controllable Quality Factor and Circular Dichroism. *Nano Lett.* **2025**, *25*, 2519–2527.

[32] N. D. Le, P. Bouteyre, A. Kheir-Aldine, F. Dubois, S. Cueff, L. Berguiga, X. Letartre, P. Viktorovitch, T. Benyattou, H. S. Nguyen. Super Bound States in the Continuum on a Photonic Flatband: Concept, Experimental Realization, and Optical Trapping Demonstration. *Phys. Rev. Lett*. **2024**, *132*, 1738022.

[33] M. Li, Y. Liu, L. Tao, S. Ma, Y. Dong, Z. Li, L. Du, Y. Guo, K. Song, X. Zhao. Evolution of an Overlapped Bandgap and Topological Flat Bands in a Higher-Order Valley Photonic Insulator Based on Dendritic Structure. *Laser Photonics Rev.* **2024**, *18*, 2300923.

[34] H. S. Nguyen, F. Dubois, T. Deschamps, S. Cueff, A. Pardon, J. L. Leclercq, C. Seassal, X. Letartre, P. Viktorovitch. Symmetry Breaking in Photonic Crystals: On-Demand Dispersion from Flatband to Dirac Cones. *Phys. Rev. Lett*. **2018**, *120*, 066102.

[35] M. Choi, C. Munley, J. E. Froch, R. Chen, A. Majumdar. Nonlocal, Flat-Band Meta-Optics for Monolithic, High-Efficiency, Compact Photodetectors. *Nano Lett.* **2024**, *24*, 3150–3156.

[36] A. C. Overvig, M. Cotrufo, M. Markowitz, Y. Zhou, B. Hao, K. Stensvad, C. Schardt, A. Alù. Zone-Folded Quasi-bound State Metasurfaces with Customized, Symmetry-Protected Energy-Momentum Relations. *ACS Photonics* **2023**, *10*, 1832–1840.

[37] T. T. H. Do, Z. Yuan, E. G. Durmusoglu, H. K. Shamkhi, V. Valuckas, C. Zhao, A. I. Kuznetsov, H. V. Demir, C. Dang, H. S. Nguyen, S. T. Ha. Room-Temperature Lasing at Flatband Bound States in the Continuum. *ACS Nano* **2025**, *19*, 19287–19296.

[38] S. Eyvazi, E. A. Mamonov, R. Heilmann, J. Cuerda, P. Torma. Flat-Band Lasing in Silicon Waveguide-Integrated Metasurfaces. *ACS Photonics* **2025**, *12*, 1570–1578.

[39] K. Sun, Y. Cai, L. Huang, Z. Han. Ultra-narrowband and rainbow-free mid-infrared thermal emitters enabled by a flat band design in distorted photonic lattices. *Nat. Commun.* **2024**, *15*, 4019.

[40] K. Sun, G. Wang, W. Li, Y. Wang, Y. Cai, L. Huang, A. Alu, Z. Han. Full polarization and high coherence control of thermal emissions via saddle-band dispersion engineering. *Nat. Commun.* **2025**, *16*, 8393.

[41] K. Sun, B. Yang, Y. Cai, Y. Kivshar, Z. Han. Circularly polarized thermal emission driven by chiral flatbands in monoclinic metasurfaces. *Sci. Adv.* **2025**, *11*, eadw0986.

[42] C. U. Hail, L. Michaeli, H. A. Atwater. Third Harmonic Generation Enhancement and Wavefront Control Using a Local High-Q Metasurface. *Nano Lett.* **2024**, *24*, 2257–2263.

[43] L. Huang, W. Zhang, X. Zhang. Moire Quasibound States in the Continuum. *Phys. Rev. Lett*. **2022**, *128*, 253901.

[44] K. Sun, K. Wang, W. Wang, Y. Cai, L. Huang, A. Alù, Z. Han. High-Q photonic flat-band resonances for enhancing third-harmonic generation in all-dielectric metasurfaces. *Newton*

2025, *1*, 100057.

[45] X. Wang, Z. Liu, B. Chen, G. Qiu, D. Wei, J. Liu. Experimental Demonstration of High-Efficiency Harmonic Generation in Photonic Moire Superlattice Microcavities. *Nano Lett.* **2024**, *24*, 11327–11333.

[46] M. Choi, A. Alù, A. Majumdar. Observation of Photonic Chiral Flatbands. *Phys. Rev. Lett.* **2025**, *134*, 103801.

[47] S. Yu, Y. Sun, D. Y. Choi, Z. Li, W. Liu, W. Zhou, H. Cheng, S. Chen. Enhancing the Quality Factors of Guided Resonances via Rational Symmetry Breaking. *Laser Photonics Rev.* **2025**, e01799.

[48] W. Wang, Y. K. Srivastava, T. C. Tan, Z. Wang, R. Singh. Brillouin zone folding driven bound states in the continuum. *Nat. Commun.* **2023**, *14*, 2811.

[49] Y. Zhang, L. Wang, H. He, H. Duan, J. Huang, C. Gao, S. You, L. Huang, A. E. Miroshnichenko, C. Zhou. High-Q magnetic toroidal dipole resonance in all-dielectric metasurfaces. *APL Photon.* **2024**, *9*, 7.

Decoupled control of the quality (Q) factor and circular dichroism (CD) of intrinsic chiral quasi-guided modes (QGMs) over a broad wavevector range is achieved in a partially etched dielectric metasurface, enabling angle-insensitive linear and nonlinear CD and providing a versatile platform for next-generation functional chiral metasurfaces.

Yuexin Sun, Shiwang Yu, Guangzhou Geng, Zhancheng Li*, Yanchun Wang, Wenwei Liu, Hui Liu, Qiang Li, Junjie Li, Hua Cheng*, and Shuqi Chen*

Photonic intrinsic chiral flatband with tailorable quality factor and circular dichroism

ToC figure: